

Gain-assisted harmonic generation in near-zero permittivity metamaterials made of plasmonic nanoshells

This article has been downloaded from IOPscience. Please scroll down to see the full text article.

2012 New J. Phys. 14 103016

(<http://iopscience.iop.org/1367-2630/14/10/103016>)

View [the table of contents for this issue](#), or go to the [journal homepage](#) for more

Download details:

IP Address: 24.96.62.248

The article was downloaded on 24/10/2012 at 02:41

Please note that [terms and conditions apply](#).

Gain-assisted harmonic generation in near-zero permittivity metamaterials made of plasmonic nanoshells

**Maria Antonietta Vincenti^{1,4,5}, Salvatore Campione^{2,4},
Domenico de Ceglia^{1,4}, Filippo Capolino² and Michael Scalora³**

¹ Aegis Technologies Inc., 410 Jan Davis Dr., Huntsville, AL 35806, USA

² Department of Electrical Engineering and Computer Science, University of California Irvine, CA 92697, USA

³ US Army Charles M Bowden Research Center, RDECOM, Redstone Arsenal, Huntsville, AL 35898, USA

E-mail: mvincenti@aegistg.com

New Journal of Physics **14** (2012) 103016 (18pp)

Received 28 July 2012

Published 9 October 2012

Online at <http://www.njp.org/>

doi:10.1088/1367-2630/14/10/103016

Abstract. We investigate enhanced harmonic generation processes in gain-assisted, near-zero permittivity metamaterials composed of spherical plasmonic nanoshells. We report the presence of narrow-band features in transmission, reflection and absorption induced by the presence of an active material inside the core of the nanoshells. The damping-compensation mechanism used to achieve the near-zero effective permittivity condition also induces a significant increase in field localization and strength and, consequently, enhancement of linear absorption. When only metal nonlinearities are considered, second- and third-harmonic generation efficiencies obtained by probing the structure in the vicinity of the near-zero permittivity condition approach values as high as 10^{-7} for irradiance value as low as 10 MW cm^{-2} . These results clearly demonstrate that a relatively straightforward path now exists for the development of exotic and extreme nonlinear optical phenomena in the kW cm^{-2} range.

⁴ These authors contributed equally to this work.

⁵ Author to whom any correspondence should be addressed.



Content from this work may be used under the terms of the [Creative Commons Attribution-NonCommercial-ShareAlike 3.0 licence](https://creativecommons.org/licenses/by-nc-sa/3.0/). Any further distribution of this work must maintain attribution to the author(s) and the title of the work, journal citation and DOI.

Contents

| | |
|--------------------------------------------------------------------------------------------|-----------|
| 1. Introduction | 2 |
| 2. Linear response of metamaterial slabs composed of plasmonic nanoshells | 3 |
| 3. Nonlinear response of metamaterial slabs arising from metal shells | 6 |
| 3.1. Second-harmonic generation from gold nanoshells | 7 |
| 3.2. Third-harmonic generation from gold nanoshells | 10 |
| 4. Nonlinear response of metamaterial slabs arising from bulk nonlinearities | 11 |
| 4.1. Effects of second- and third-order susceptibilities in the host medium | 12 |
| 4.2. Effects of second- and third-order susceptibilities in the nanoshells' core | 12 |
| 5. The role of gain | 13 |
| 6. Conclusions | 15 |
| References | 16 |

1. Introduction

Finite thickness metamaterials composed of sub-wavelength constitutive elements have stimulated researchers to engineer intriguing homogenized material properties, such as negative refractive index, artificial permeability and near-zero permittivity (NZP), which in turn have found applications in many practical scenarios. For example, artificial magnetism has been achieved via the split ring resonator (SRR) structure [1], initially introduced at microwave frequencies and then extrapolated to infrared frequencies by scaling the dimensions of the SRR [2, 3]. Plasmonic nanoshells arranged in periodic lattices have been investigated for their unique optical properties, such as strongly directional band gaps [4], negative refractive index [5], NZP [6–8] and various applications, such as surface enhanced Raman scattering, surface enhanced infrared absorption [9] and negative refraction [10]. Moreover, artificial composite materials exhibiting NZP capabilities [11] have attracted the attention of the scientific community in view of their potential applications, including tunneling of electromagnetic energy [12], boosting of optical nonlinearities [13], low-threshold nonlinear effects [14, 15] and producing narrow directive beams [16, 17].

The main advantage of exploiting the NZP condition to access nonlinear processes is offered by the huge field enhancement that occurs at the interface of an NZP medium. For a lossy NZP medium large field enhancement values due to the continuity requirement of the longitudinal component of the displacement field at the interface are achieved for a transverse magnetic (TM)-polarized incident wave and specific angles of incidence [12, 14]. Recently, it was demonstrated that efficient second-harmonic (SH) and third-harmonic (TH) generation may be achieved in the proximity of the zero crossing point of the real part of the dielectric permittivity without resorting to any resonant mechanism [15]. Although Vincenti *et al* [15] showed several solutions to achieve singularity-driven nonlinear processes in natural materials, losses represent a significant impediment to the triggering of low-threshold, nonlinear phenomena. An efficient way to abate damping in composite, artificial nanostructures consists in the inclusion of active media, such as dyes or quantum dots [6, 8, 18]. For example, in [6] a relative permittivity value of $\text{Im}(\epsilon) \approx 10^{-4}$ is estimated in the vicinity of the zero crossing point ($\text{Re}(\epsilon) = 0$) for an array of gold nanoshells, where silica-like cores including 10 mM of Rhodamine 800 fluorescent dyes pumped at $\lambda \approx 680$ nm provided damping compensation.

Full-wave linear simulations of the metamaterial nanostructure proposed in [6] are shown in section 2 as a function of frequency and incident angle of the incoming plane wave. Linear and nonlinear responses arising from nanoshells similar to those described in [6] that do not resort to damping compensation have been reported in [19]. The simultaneous availability of the NZP condition and damping compensation, however, complicates both linear and nonlinear responses of the nanostructure. In this paper, we aim to exploit the enhanced narrow-band processes arising from the metamaterial damping-compensation mechanism to boost the already promising theoretical results reported in [15]. We investigate the nonlinear contributions arising from the metal (section 3) and from dielectric media separately by either filling with or hosting the nanoparticles in a nonlinear medium (section 4). Although metals do not possess intrinsic, dipolar, quadratic nonlinear terms, they display an effective second-order nonlinearity that arises from a combination of symmetry breaking at the surface, magnetic response (Lorentz force), inner-core electrons, convective nonlinear sources and electron gas pressure [20]. We also consider third-order nonlinearity of the gold shells that together with effective second-order nonlinear sources contribute significantly to the generated signals [21, 22]. A detailed study of each nonlinear contribution, without making any *a priori* assumption about the relative weights of surface and volume sources, allows us to predict SH and TH conversion efficiencies of the order of 10^{-7} when probe irradiance is as low as 10 MW cm^{-2} . The inclusion of a dielectric nonlinear medium characterized by relatively low second- and third-order susceptibilities shows how to further improve conversion efficiencies, paving the way for as yet unexplored low-threshold nonlinear phenomena. Finally, in section 5 we analyze the critical role of gain-assisted harmonic generation by investigating the effect of different concentrations of the active material. This study serves also as a guide for future experimental works on the subject, where either dye concentration or pump intensity variations can modify significantly the nonlinear response of the metamaterial.

2. Linear response of metamaterial slabs composed of plasmonic nanoshells

We start our analysis by considering a composite material having finite thickness h along the z direction, made of four layers of arrayed nanoshells with period $a = 100 \text{ nm}$, embedded in a homogeneous host medium with relative permittivity $\varepsilon_h = 2.25$ (see figure 1). The composite material extends to infinity in the x and y directions, also with period a . To mitigate metamaterial losses, the core of the nanoshells is filled with glass doped with Rhodamine 800 fluorescent molecules, homogeneously modeled with relative permittivity according to the relation $\varepsilon_c = 2.25 + \varepsilon_c(\Gamma_{\text{pump}}, \bar{N}_0)$, with $\varepsilon_c(\Gamma_{\text{pump}}, \bar{N}_0)$ as in [6], assuming that the concentration of dye molecules is $\bar{N}_0 = 10 \text{ mM}$ (other concentration values will be considered in section 5), pumping rate $\Gamma_{\text{pump}} = 6.5 \times 10^9 \text{ s}^{-1}$ and core radius $r_c = 30 \text{ nm}$. Each shell is made of gold, with relative permittivity ε_s modeled through the Drude model as shown in [6], and external radius $r_s = 35 \text{ nm}$. The relationship between $\varepsilon_c(\Gamma_{\text{pump}}, \bar{N}_0)$ and the pump light intensity I_{pump} is not straightforward when the gain medium is either enclosed by a nanoshell or is close to other nano scatterers (as in the proposed case), whereas it is rather simple for an open gain medium. As a first approximation, one may consider the relation in open gain media where $I_{\text{pump}} = \Gamma_{\text{pump}} h f_{30} / \sigma_{\text{abs}}$, where σ_{abs} is the dye's absorption cross section, h is Planck's constant and f_{30} is the pump frequency [23]. For Rhodamine 800 dye molecules, $\sigma_{\text{abs}} = 3.14 \times 10^{-16} \text{ cm}^2$ and $f_{30} = 441 \text{ THz}$ [24, 25], which results in $I_{\text{pump}} = 6.5 \text{ MW cm}^{-2}$. Further improvements to the model may be based on a more extensive analysis of the electrodynamic system at the pump

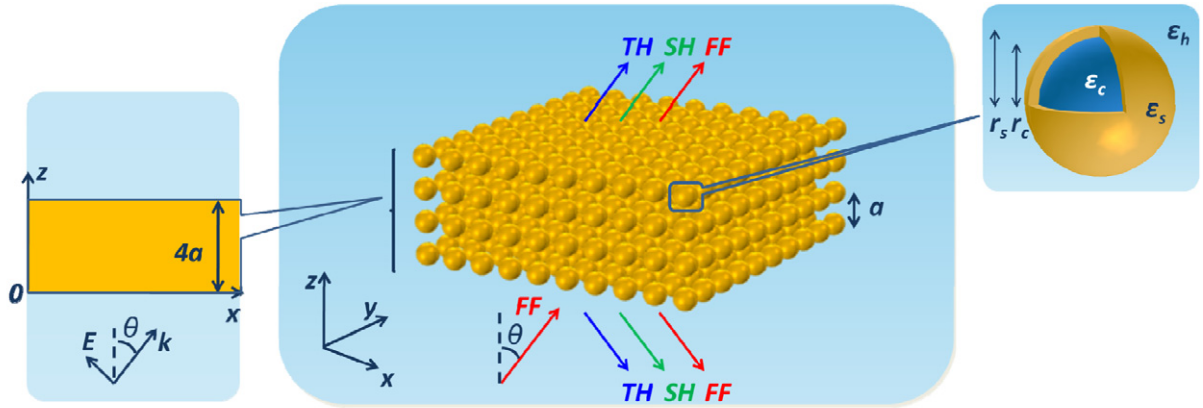


Figure 1. Sketch of the composite material with finite thickness h made of four layers of nanoshells with distance a embedded in a homogeneous medium with relative permittivity ϵ_h . The composite material extends to infinity in the x and y directions, with period a . The nanoshell core is made of glass doped with Rhodamine 800 fluorescent molecules, with homogenized relative permittivity ϵ_c and radius r_c . The shell is made of gold, with relative permittivity ϵ_s and external radius r_s . FF stands for fundamental frequency and SH and TH stand for second and third harmonic, respectively.

frequency and on determining local pump fields and local absorption. We note that the analysis carried out here is performed in the steady state. A more extensive analysis that includes pulsed dynamics and rate equations [23] will be implemented in a future work.

We assume a pump/probe optical setup: the pump, used to activate the dye molecules and set the metamaterial in gain condition, is tuned at $\lambda = 680$ nm (corresponding to 441 THz) and leads to the linear response shown in figure 2; we will define the details of the probe signal for the harmonic processes in sections 3 and 4. More details of the design of the metamaterial under investigation may be found in [6]. The main feature of the proposed structure is the achievement of efficient damping compensation in the vicinity of the zero crossing point of the real part of the metamaterial effective dielectric constant. These two conditions, in fact, are not coincident in frequency: an effective $\text{Im}(\epsilon) \approx 10^{-4}$ is obtained for $\lambda \approx 712$ nm, while $\text{Re}(\epsilon) \approx 0$ at $\lambda \approx 710.6$ nm. The effective permittivity has been calculated by means of the Nicolson–Ross–Weir method applied to a metamaterial slab of finite thickness under normal incidence conditions [26, 27].

The metamaterial slab is illuminated with a TM-polarized plane wave, incident at an angle θ with respect to the z -axis, with electric field and wavevector lying in the x - z plane (figure 1). Transmission, reflection and absorption as functions of wavelength and incident angle are shown in figure 2, calculated using two different methods but yielding similar results: a single dipole approximation (SDA; figures 2(a), (c) and (e)) and a full-wave simulation based on a finite-element method in the frequency domain (COMSOL Multiphysics; figures 2(b), (d) and (f)). The SDA approach [28–30] assumes that each nanoshell behaves as an electric dipole, with induced electric dipole moment $\mathbf{p} = \alpha_{ee} \mathbf{E}^{\text{loc}}$, where α_{ee} is the electric polarizability modeled via the Mie theory [28] and \mathbf{E}^{loc} is the local field acting on it. The SDA is a good approximation when the plasmonic nanoshells are used close to their fundamental plasmonic frequency, when particle dimensions are much smaller than the incident wavelength, and when the

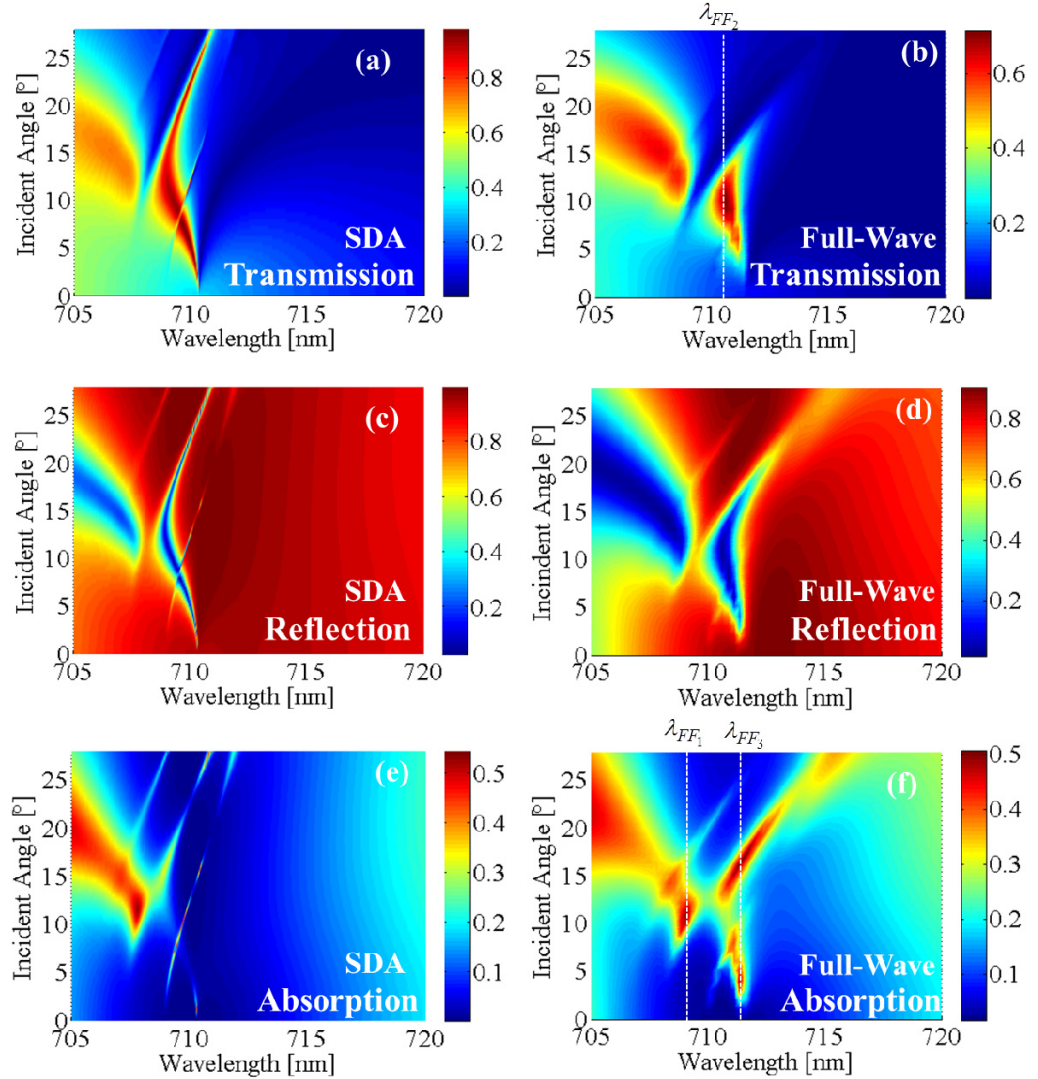


Figure 2. Transmission ((a), (b)), reflection ((c), (d)) and absorption ((e), (f)) as a function of wavelength and incident angle calculated via the SDA approach and full-wave (finite element method) simulation as noted, for the damping-compensated metamaterial slab in figure 1.

period $a \geq 3r_s$. In general, more accurate results may be obtained by including multipole field contributions [28, 31–33].

As shown in figure 1, we model $N = 4$ layers of nanoshells embedded in a homogeneous environment. Let us consider a reference nanoshell located at the n th layer $\mathbf{r}_n = x_0\hat{\mathbf{x}} + y_0\hat{\mathbf{y}} + z_{0,n}\hat{\mathbf{z}}$ (we can assume that $x_0 = 0$, $y_0 = 0$ and $z_{0,n} = na - a/2$, with $n = 1, \dots, 4$). The local electric field acting on it is given by $\mathbf{E}^{\text{loc}}(\mathbf{r}_n) = \mathbf{E}^{\text{inc}}(\mathbf{r}_n) + \sum_{m=1}^4 \mathbf{G}_{n,m}^{\text{layer}} \cdot \mathbf{p}_m$, where $\mathbf{E}^{\text{inc}}(\mathbf{r}) = \mathbf{E}_0 e^{i\mathbf{k} \cdot \mathbf{r}}$ is the TM incident electric field with the wavevector \mathbf{k} lying in the x - z plane, and \mathbf{p}_m , $m = 1, \dots, N$, are the electric dipole moments at positions \mathbf{r}_m . Furthermore, the term $\mathbf{G}_{n,m}^{\text{layer}} \equiv \mathbf{G}^\infty(\mathbf{r}_n, \mathbf{r}_m)$, for $n \neq m$, represents the periodic dyadic Green's function (PDGF) for a two-dimensional periodic array of dipoles [34, 35], whereas $\mathbf{G}_{n,n}^{\text{layer}} \equiv \tilde{\mathbf{G}}^\infty(\mathbf{r}_n, \mathbf{r}_n)$ represents its regularized counterpart (without the contribution from the dipole at \mathbf{r}_n) [34, 35]. Both

$\underline{\mathbf{G}}^\infty$ and $\underline{\mathbf{G}}^\infty$ are evaluated through the Ewald method [36, 37] that provides: (i) rapid converging summations (only a handful of summation terms is needed to achieve convergence) and (ii) analytic continuation to the complex wavenumber plane. The Ewald method for the two-dimensional periodic array of scalar Green's functions is detailed in [38–40]. Following the formulation in sections III.C and III.D of [35], we then calculate the induced dipole moments \mathbf{p}_n , $n = 1, \dots, 4$, by solving the four combined linear equations $\sum_{m=1}^4 \underline{\mathbf{A}}_{n,m} \cdot \mathbf{p}_m = \alpha_{ee} \mathbf{E}^{\text{inc}}(\mathbf{r}_n)$, where $\underline{\mathbf{A}}_{n,m} = -\alpha_{ee} \underline{\mathbf{G}}_{n,m}^{\text{layer}}$, for $n \neq m$, and $\underline{\mathbf{A}}_{n,n} = \mathbf{I} - \alpha_{ee} \underline{\mathbf{G}}_{n,n}^{\text{layer}}$. Once the solution \mathbf{p}_n has been determined, reflection and transmission coefficients are simply evaluated using again the PDGFs $\underline{\mathbf{G}}^\infty(\mathbf{r}, \mathbf{r}_n)$. A slight blue shift in the results retrieved via SDA with respect to the full-wave COMSOL result (see figure 2) is observed. Also, transmission, reflection and absorption values are slightly different in the SDA case because we are not taking into account the multipolar response. However, similar spectral and angular features are clearly observed in both cases in figure 2. The presence of a damping-compensation mechanism, or more generally NZP condition in the presence of low losses [41], allows the occurrence of narrow-band features and boosts electric field values. We stress that we do not treat the metamaterial as a homogenized slab with effective parameters, since for any incident angle and wavelength the field localization inside the metamaterial slab varies substantially and thus leads to different nonlinear responses.

In order to investigate the more general behavior of the structure in the proximity of the $\text{Re}(\epsilon) \approx 0$ condition, we calculated the induced dipole moment $\mathbf{p} = p_x \hat{\mathbf{x}} + p_z \hat{\mathbf{z}}$ in the x and z directions at the section $z = 3a/2$, which corresponds to the second bottom layer of nanoshells (figure 3). Inspection of figure 3 reveals that in the vicinity of the NZP condition, the magnitude of the longitudinal component of the induced dipole moment p_z (figure 3(a)) is much larger than the transverse component p_x (figure 3(b)), which remains small. By looking at the phase of the induced dipole moment in the same spectral/angular region, one may also note that the $\text{Re}(\epsilon) \approx 0$ condition causes a π -shift in the phase of the longitudinal component, while no phase shift is observed for the transverse component. These conditions may be important in phase-sensitive processes such as harmonic generation and optical bistability.

A key aspect for the purposes of efficient harmonic generation and low-threshold optical bistability processes is electric field enhancement inside the structure. We used a full-wave approach to calculate the electric field intensity enhancement, defined as $\text{EF} = \max(|\mathbf{E}|^2/|\mathbf{E}^{\text{inc}}|^2)$, where $|\mathbf{E}|$ is the total electric field magnitude inside the metamaterial slab and $|\mathbf{E}^{\text{inc}}|$ is the electric field magnitude of the incident plane wave. Our calculations predict the following electric field enhancements: $\text{EF} \approx 1000$ at $\lambda_{\text{FF}_1} = 709.5$ nm and $\theta = 13^\circ$; $\text{EF} \approx 1900$ at $\lambda_{\text{FF}_2} = 710.6$ nm and $\theta = 7^\circ$; and $\text{EF} \approx 3000$ at $\lambda_{\text{FF}_3} = 711.35$ nm and $\theta = 4^\circ$, with angular trends that match well the shape of the absorption profile in the structure (see figure 2(f)). Although high field enhancement values are promising for efficient nonlinear processes, one should keep in mind that nonlocal effects may intervene for small metal thicknesses, as may be the case for a 5 nm thick gold shell. However, in what follows, we will assume that nonlocal effects are either negligible or may be compensated for with higher concentrations of gain material, and we postpone this discussion to a future effort.

3. Nonlinear response of metamaterial slabs arising from metal shells

We now consider a pump–probe scenario, where we assume that a continuous wave (CW) pump signal keeps the system in the damping-compensation regime described in the previous section.

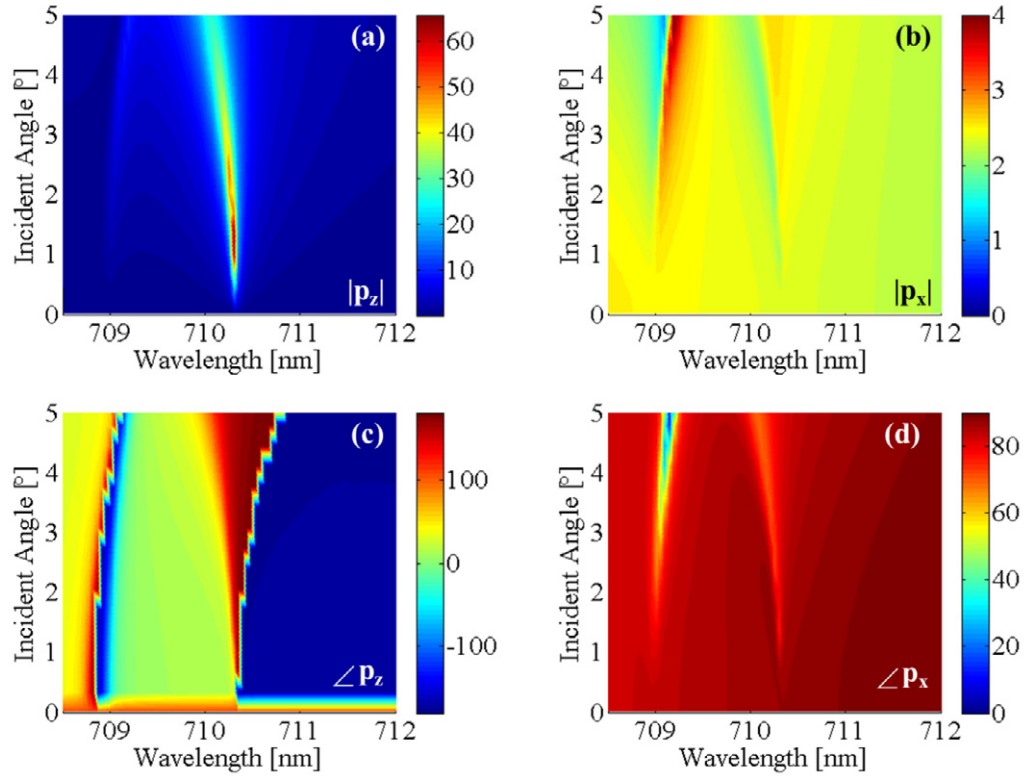


Figure 3. Induced dipole moment magnitude in (a) the z direction and (b) the x direction at $z = 3a/2$ for the metamaterial slab in figure 1. Induced dipole moment phase in (c) the z direction and (d) the x direction at $z = 3a/2$ for the metamaterial slab in figure 1. These results have been obtained by the SDA approach.

We then assume a time harmonic probe signal with irradiance 10 MW cm^{-2} and calculate its second and third generated harmonics. This relatively small irradiance guarantees that the probe will remain undepleted so that we may neglect any self-phase modulation and down-conversion processes in our calculations. Here we also neglect any self-phase modulation of the pump signal and cross-phase modulation between pump and probe signals. Moreover, we expect that harmonic generated signals triggered by the pump field will not significantly alter the harmonic generation conversion efficiencies relative to the probe frequency for two reasons: (i) both the pump and the probe are CW signals so that their harmonics will fall at different frequencies and (ii) the pump signal is tuned in a spectral region where the metamaterial absorbs and no substantial field enhancement is expected. For these reasons, in what follows, we will neglect the pump contribution to harmonic generation associated with the probe signal.

3.1. Second-harmonic generation from gold nanoshells

The nonlinear contributions to second-harmonic generation (SHG) arising from the metal come mostly from free electrons [20, 42, 43]. The hydrodynamic model is used to describe free-electron motion, and we do not make any assumptions on the relative weight of surface and volume contributions. A nonlinear equation of motion for the current density of free electrons

may be written in the time domain as follows (a tilde (\sim) is used to denote quantities in the time domain) [20, 42, 43]:

$$\frac{\partial \tilde{\mathbf{J}}_f}{\partial t} + \gamma_f \tilde{\mathbf{J}}_f = \varepsilon_0 \omega_p^2 \tilde{\mathbf{E}} + \frac{1}{n_0 e} \left[\tilde{\mathbf{J}}_f \nabla \cdot \tilde{\mathbf{J}}_f + \left(\tilde{\mathbf{J}}_f \cdot \nabla \right) \tilde{\mathbf{J}}_f \right] - \frac{\mu_0 e}{m^*} \tilde{\mathbf{J}}_f \times \tilde{\mathbf{H}}, \quad (1)$$

where $\tilde{\mathbf{J}}_f$ is the free-electron current density, $\gamma_f = 7.28 \times 10^{13} \text{ s}^{-1}$ is the damping coefficient associated with gold losses, e is the electron charge, $m^* = 9.109 \times 10^{-31} \text{ kg}$ is the effective electron mass, μ_0 is the vacuum magnetic permeability, $n_0 = 4.963 \times 10^{22} \text{ cm}^{-3}$ is the conduction electron density and $\tilde{\mathbf{H}}$ and $\tilde{\mathbf{E}}$ are the local magnetic and electric fields, respectively.

We transform equation (1) into the frequency domain by expressing all the variables as superposition of two components, one oscillating at the fundamental wavelength and the other oscillating at the SH frequency. We may write the following frequency-domain expression for the current density at the SH frequency:

$$\mathbf{J}_{\text{SH}} = -i\varepsilon_0 [\varepsilon_s(\omega_{\text{SH}}) - 1] \omega_{\text{SH}} \mathbf{E}_{\text{SH}} + \mathbf{J}_{\text{vol}} + \mathbf{J}_{\text{surf}}. \quad (2)$$

The first term on the right-hand side of equation (2) is the linear response at the SH angular frequency ω_{SH} due to both free and bound electrons, and depends on the experimental permittivity of gold at the SH frequency $\varepsilon_s(\omega_{\text{SH}})$. The second (\mathbf{J}_{vol}) and third (\mathbf{J}_{surf}) terms are bulk and surface nonlinear contributions due to free electrons. These source terms may be derived within the context of the hydrodynamic model in equation (1), following the method illustrated in [44, 45] for vacuum-metal interfaces, which is adapted to take into account absorption losses in the metal and the effects of a generic dielectric with permittivity ε_B in contact with metal as detailed in [46],

$$\mathbf{J}_{\text{vol}} = i\omega_{\text{SH}}\varepsilon_0 \frac{e}{2m^*\omega_{\text{FF}}^2} \frac{[\varepsilon_{s,f}(\omega_{\text{FF}}) - 1]}{2} \beta \left[(\alpha - 1) (\mathbf{E}_{\text{FF}} \cdot \nabla) \mathbf{E}_{\text{FF}} + \frac{1}{2} \nabla (\mathbf{E}_{\text{FF}} \cdot \mathbf{E}_{\text{FF}}) \right], \quad (3)$$

$$\hat{\mathbf{t}} \cdot \mathbf{J}_{\text{surf}} = -i\omega_{\text{SH}}\varepsilon_0 \chi_{\parallel}^{(2)} E_{\text{FF},\parallel} E_{\text{FF},\perp}, \quad (4)$$

$$\hat{\mathbf{n}} \cdot \mathbf{J}_{\text{surf}} = -i\omega_{\text{SH}}\varepsilon_0 \chi_{\perp}^{(2)} E_{\text{FF},\perp}^2.$$

In expressions (3) and (4) ω_{FF} is the fundamental angular frequency, $\varepsilon_{s,f}(\omega_{\text{FF}}) = -(e^2 n_0 / m^*) / (\omega_{\text{FF}}^2 + i\omega_{\text{FF}}\gamma_f)$ is the free-electron permittivity, $\alpha = \omega_{\text{FF}} / (\omega_{\text{FF}} + i\gamma_f)$, $\beta = \omega_{\text{SH}} / (\omega_{\text{SH}} + i\gamma_f)$ and \mathbf{E}_{FF} is the electric field at the fundamental frequency; $\hat{\mathbf{t}}$ and $\hat{\mathbf{n}}$ define a local, boundary coordinate system and represent unit vectors pointing in the directions tangential and outward normal to the metallic surfaces, respectively; $E_{\text{FF},\parallel}$ and $E_{\text{FF},\perp}$ are the magnitudes of the tangential and normal electric field components at the fundamental frequency in this local coordinate system. The surface, quadratic nonlinear susceptibilities are then given by

$$\chi_{\parallel}^{(2)} = -\alpha\beta \frac{e}{2m^*\omega_{\text{FF}}^2} \left[\frac{\varepsilon_s (\varepsilon_B - 1) + \varepsilon_B (1 - \varepsilon_{s,f}(\omega_{\text{FF}}))}{\varepsilon_B} \right], \quad (5)$$

$$\chi_{\perp}^{(2)} = -\alpha\beta \frac{e}{2m^*\omega_{\text{FF}}^2} \left[\frac{3\varepsilon_s^2 (\varepsilon_B - 1) + \varepsilon_B \varepsilon_s (\varepsilon_B - \varepsilon_{s,f}(\omega_{\text{FF}})) + 3\varepsilon_B^2 (1 - \varepsilon_{s,f}(\omega_{\text{FF}}))}{4\varepsilon_B^2} \right],$$

where ε_B assumes the value ε_c or ε_h depending on whether the inner or outer interface of the shell is considered for $\chi_{\parallel}^{(2)}$ and $\chi_{\perp}^{(2)}$ calculations.

In figure 4 we show the forward, backward and total (i.e. forward plus backward) SH conversion efficiencies calculated as $\eta_{\text{SH}} = P_{2\omega} / P_{\omega}$, where P_{ω} is the input probe power

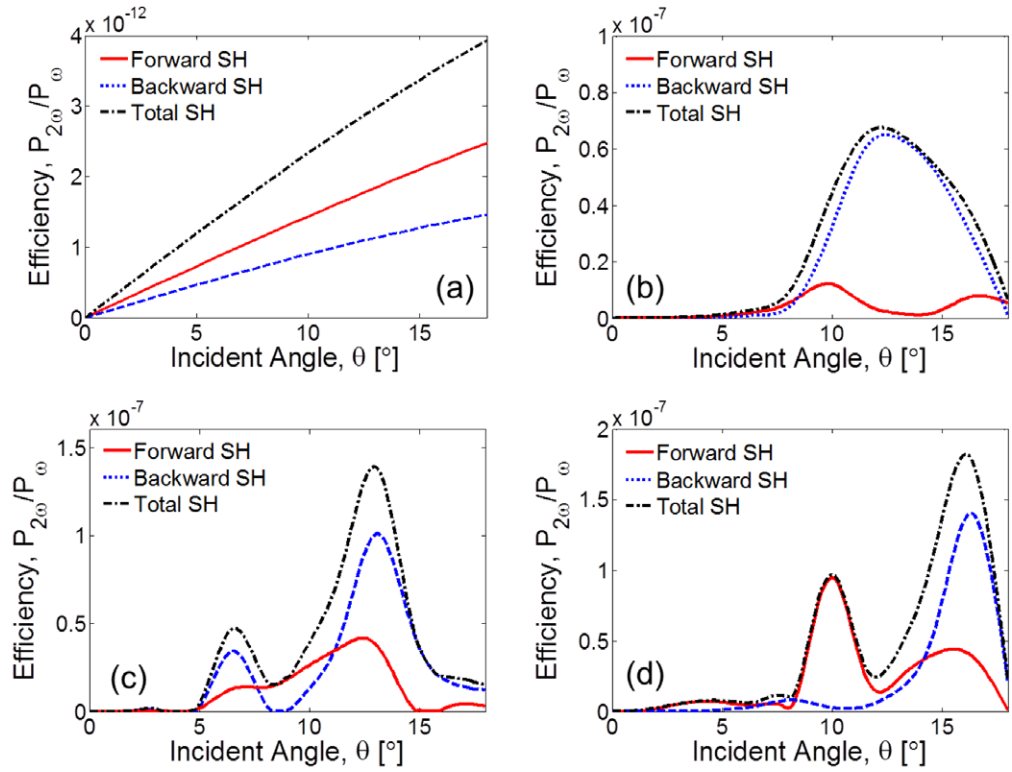


Figure 4. Forward, backward and total (calculated as forward plus backward) second harmonic conversion efficiency $\eta_{SH} = P_{2\omega}/P_{\omega}$ for (a) 5 nm thick flat gold, (b) NZP metamaterial described in section 2 at $\lambda_{FF_1} = 709.5$ nm, (c) at $\lambda_{FF_2} = 710.6$ nm and (d) at $\lambda_{FF_3} = 711.35$ nm as a function of incident angle. Note the five orders of magnitude increase when using the metamaterial in section 2. These results have been calculated by means of full-wave (finite element method) simulations.

and $P_{2\omega}$ is the radiated power (in the forward, backward or forward plus backward directions) at the SH [47]. We analyzed three different wavelengths where either absorption or transmission peaked ($\lambda_{FF_1} = 709.5$ nm—figure 2(f); $\lambda_{FF_2} = 710.6$ nm—figure 2(b); $\lambda_{FF_3} = 711.35$ nm—figure 2(f)). The results in figures 4(b)–(d) reveal a dramatic increase of the generated signal by at least five orders of magnitude when compared with a flat gold film (figure 4(a)) having the same thickness as the shell (5 nm). Moreover, we note that forward and backward harmonic efficiencies are strongly modulated as the incident angle varies. In particular, while one may certainly surmise a relationship between the trends of linear absorption and total SH generation, it is not straightforward to establish a one-to-one relation between the maxima of the forward and backward harmonic processes and absorption or transmission profile. Field localization and phase accumulation at the probe (the probe is tuned in a region where phase accumulation is close to zero) and harmonic frequencies assume completely different character for each peak of transmission/absorption for the probe, so that forward and backward harmonic generation arising from both surface and volume contributions should be examined on a case-by-case basis and cannot be merely inferred from the linear response of the structure. A rough estimation of the *effective second-order nonlinear*

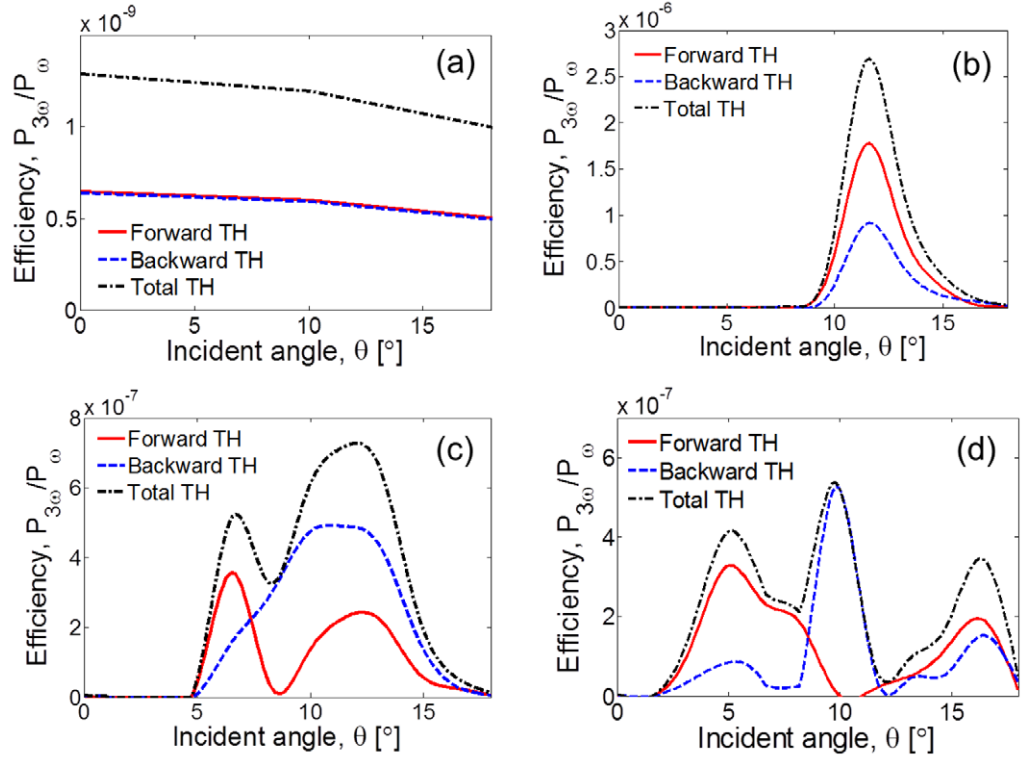


Figure 5. Forward, backward and total (calculated as forward plus backward) third harmonic conversion efficiency $\eta_{\text{TH}} = P_{3\omega}/P_{\omega}$ for (a) 5 nm thick flat gold, (b) NZP metamaterial described in section 2 at $\lambda_{\text{FF}_1} = 709.5$ nm, (c) at $\lambda_{\text{FF}_2} = 710.6$ nm and (d) at $\lambda_{\text{FF}_3} = 711.35$ nm as a function of incident angle. Note the three orders of magnitude increase when using the metamaterial in section 2. These results have been calculated by means of full-wave (finite element method) simulations.

susceptibility that comes from symmetry breaking at the surface, magnetic dipoles, inner-core electrons and convective nonlinear sources may be obtained by replacing these terms with a $\chi_{\text{eff}}^{(2)} \sim 5000 \text{ pm V}^{-1}$. This value gives the reader an idea of the kind of field enhancement that is achieved inside each gold nanoshell.

3.2. Third-harmonic generation from gold nanoshells

Like all other metals, gold possesses a relatively large third-order nonlinearity. However, different material configurations, growth techniques and pulse duration have led to a disparate set of values for the third-order susceptibility, ranging from 10^{-14} to $10^{-19} \text{ m}^2 \text{ V}^{-2}$ [48–50]. Since we are not specifically interested in quantifying or optimizing conversion efficiency values and instead wish to explore the nonlinear optical properties triggered by the NZP and damping-compensation regimes, in what follows we assume that $\chi_{xxxx}^{(3)} = \chi_{yyyy}^{(3)} = \chi_{zzzz}^{(3)} = 10^{-17} \text{ m}^2 \text{ V}^{-2}$ (all other tensor components are assumed to be zero). As we did for SHG, here too we calculate forward, backward and total TH signals at $\lambda_{\text{FF}_1} = 709.5$ nm (figure 5(b)), $\lambda_{\text{FF}_2} = 710.6$ nm (figure 5(c)), and $\lambda_{\text{FF}_3} = 711.35$ nm (figure 5(d)). Conversion efficiency is calculated as

$\eta_{\text{TH}} = P_{3\omega}/P_{\omega}$, where $P_{3\omega}$ and P_{ω} are the radiated power at the TH frequency and the input probe power [47], respectively. A cursory examination of figure 5 reveals an increase of the generated TH signal from the nanocomposite metamaterial by about three orders of magnitude when compared with a flat gold film of the same thickness as the shell (5 nm) in figure 5(a). As mentioned above, care should be exercised when relating the features of linear and nonlinear processes. The highly selective angular and spectral features found in both linear and harmonic responses may indeed be ascribed to different mechanisms taking place inside the structure. An investigation of the field distribution inside the structure reveals that a number of resonant modes (three in this case) and an impedance matching condition may be identified in this structure, all leading to different degrees of field localization across the slab and consequently different harmonic responses. Moreover, different phase accumulations in the structure due to the NZP regime where the probe is tuned, together with the difference in parity and phases of the excited resonant modes, may in turn either maximize or abate field overlap, leading to complicated harmonic angular responses and differences between forward and backward generated signals. Moreover, a different angular dependence of TH signals (figure 5) when compared to SH (figure 4) is also expected based on the different trends of the two nonlinear processes for the 5 nm thick flat gold film (compare figure 4(a) with figure 5(a)) and on the fact that they arise either from surface and volume terms or solely from bulk contributions.

4. Nonlinear response of metamaterial slabs arising from bulk nonlinearities

One may now ask the following questions: (i) how does the nonlinear response change if dielectric bulk nonlinearities are also considered in the calculations? (ii) What is the relative importance of dielectric versus metal nonlinearities, and how much does each contribute to the generated signals? In this section, we will attempt to answer these questions by simulating the effect of bulk nonlinearities associated with the dielectric materials in the system, i.e. host medium and shells' core, and by comparing these results with the radiated SH and TH arising only from the gold shells.

To account for nonlinear effects in the host and core dielectrics, we express the leading contributions of the nonlinear polarization densities in the j direction at second ($P_{\text{SH},j}$) and third ($P_{\text{TH},j}$) harmonic frequencies as [47]

$$P_{\text{SH},j} = \varepsilon_0 \sum_{l,m=1}^3 \chi_{jlm}^{(2)}(\omega_{\text{SH}}, \omega_{\text{FF}}, \omega_{\text{FF}}) E_{\text{FF},l} E_{\text{FF},m},$$

$$P_{\text{TH},j} = \varepsilon_0 \sum_{l,m,n=1}^3 \chi_{jlmn}^{(3)}(\omega_{\text{TH}}, \omega_{\text{FF}}, \omega_{\text{FF}}, \omega_{\text{FF}}) E_{\text{FF},l} E_{\text{FF},m} E_{\text{FF},n},$$
(6)

where j, l, m, n are the Cartesian coordinates, ε_0 is the vacuum electric permittivity and $\chi_{jlm}^{(2)}$ and $\chi_{jlmn}^{(3)}$ are the instantaneous second- and third-order susceptibility tensors' components, respectively, and ω_{TH} is the TH angular frequency. In what follows, we will consider $\chi_{xxxx}^{(3)} = \chi_{yyyy}^{(3)} = \chi_{zzzz}^{(3)} = \chi_h^{(3)} = \chi_c^{(3)} = 10^{-21} \text{ m}^2 \text{ V}^{-2}$, values compatible with commercial glasses [47], where the subscript 'h' and 'c' stand for the host and core, respectively, and we assume a relatively low second-order susceptibility value, i.e. $\chi_{xxx}^{(2)} = \chi_{yyy}^{(2)} = \chi_{zzz}^{(2)} = \chi_h^{(2)} = \chi_c^{(2)} = 10 \text{ pm V}^{-1}$ (all other tensor components are assumed to be zero).

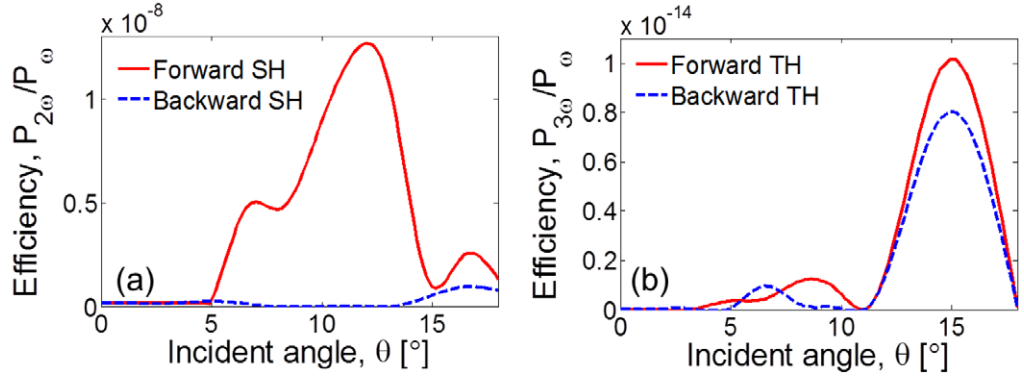


Figure 6. Forward and backward (a) SH and (b) TH conversion efficiencies for the metamaterials described in section 2 at $\lambda_{\text{FF}_2} = 710.6 \text{ nm}$ as a function of incident angle. We assume that $\chi_h^{(2)} = 10 \text{ pm V}^{-1}$ and $\chi_h^{(3)} = 10^{-21} \text{ m}^2 \text{ V}^{-2}$ for the host medium. These results have been calculated by means of full-wave (finite element method) simulations.

4.1. Effects of second- and third-order susceptibilities in the host medium

We begin our study by first introducing second- and third-order susceptibilities in the host medium (indicated by ϵ_h in figure 1). The nonlinear susceptibilities are included only in the four-period-thick region that actually contains the nanoshells and are set to zero outside. In order to identify the relative nonlinear contribution, we neglect all nonlinear terms in the metal described in the previous section. We consider the same probe irradiance (10 MW cm^{-2}) and incident wavelength, $\lambda_{\text{FF}_2} = 710.6 \text{ nm}$, where $\text{Re}(\epsilon) = 0$. Our nonlinear calculations (figure 6) reveal that both SH and TH have different angular trends when compared with figure 4(c). Moreover, we note that the SH signal radiated by the metal (figure 4(c)) exceeds the SH generated from the host medium (shown in figure 6(a)) by one order of magnitude, while the third-harmonic generation (THG) that arises from the host medium is negligible compared to the TH signal that emanates from the metal (figure 5(c)).

4.2. Effects of second- and third-order susceptibilities in the nanoshells' core

We repeat the calculations shown in section 4.1 by considering non-zero second- and third-order susceptibilities in the cores of the nanoshells: $\chi_{xxx}^{(2)} = \chi_{yyy}^{(2)} = \chi_{zzz}^{(2)} = \chi_c^{(2)} = 10 \text{ pm V}^{-1}$ and $\chi_{xxxx}^{(3)} = \chi_{yyyy}^{(3)} = \chi_{zzzz}^{(3)} = \chi_c^{(3)} = 10^{-21} \text{ m}^2 \text{ V}^{-2}$; the probe irradiance is 10 MW cm^{-2} and wavelength is $\lambda_{\text{FF}_2} = 710.6 \text{ nm}$. Just as before, in this scenario SH and TH signals manifest yet a different trend when compared with the same signals arising from the metal and from bulk nonlinearities of the host medium external to the nanoshell. In this case, SH generation becomes less efficient when only the core of the nanoshells is assumed to be nonlinear (see figure 7, in contrast to the case analyzed in section 4.1 where the host medium is nonlinear). On the other hand, the core-nonlinearity boosts THG by approximately one order of magnitude compared to the case of section 4.1 (see figure 7 for comparison). These contrasting trends in SHG and THG are most likely due to the substantial difference in field localization. For example, at $\lambda_{\text{FF}_2} = 710.6 \text{ nm}$ the electric field is well localized inside the gold shell, which

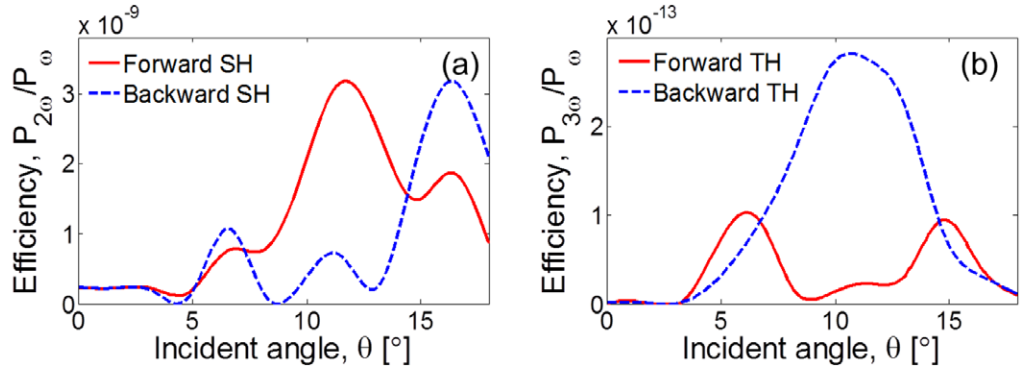


Figure 7. Forward and backward (a) SH and (b) TH conversion efficiencies for the metamaterials described in section 2 at $\lambda_{\text{FF}_2} = 710.6 \text{ nm}$ as a function of incident angle. We assumed $\chi_c^{(2)} = 10 \text{ pm V}^{-1}$ and $\chi_c^{(3)} = 10^{-21} \text{ m}^2 \text{ V}^{-2}$ inside the cores of the nanoshells. These results have been calculated by means of full-wave (finite element method) simulations.

makes the SH signal significantly larger when the metal nonlinearity is retained. The same field localization arguments cannot be applied directly to the improvements noted for the TH signal because the third-order nonlinearity of the metal is at least four orders of magnitude larger compared to the host or core dielectric's third-order nonlinearity, a discrepancy that could account for most of the improvements that we calculate.

5. The role of gain

In order to stress the key role of damping-compensation processes in shaping the linear properties to enhance electric field localization to lower nonlinear thresholds, we also calculate transmission, reflection and absorption values for the same structure sketched in figure 1 by assuming different gain conditions. We first compare the absorption maps obtained with full-wave simulations for nanoshells that contain a silica core doped with Rhodamine 800 with decreasing concentrations: 10 mM (figure 8(a)), 7 mM (figure 8(b)), 3 mM (figure 8(c)) and 0 mM (figure 8(d)). Under the same probing conditions the absorption profiles change dramatically while the $\text{Re}(\epsilon) = 0$ condition red-shifts from $\lambda \approx 710.6 \text{ nm}$ at 10 mM to $\lambda \approx 714.3 \text{ nm}$ at 7 mM and from $\lambda \approx 715.9 \text{ nm}$ at 3 mM to $\lambda \approx 717.7 \text{ nm}$ for 0 mM. We stress that the $\text{Re}(\epsilon) = 0$ conditions for different concentrations are determined by means of the Nicolson–Ross–Weir method applied to a metamaterial slab of finite thickness under normal incidence conditions [26, 27]. By comparing the results in figure 8 one may clearly infer that the majority of the features that characterize absorption (and implicitly also reflection and transmission—not shown here) arise from the ability to compensate for damping in the metamaterial. Although a predominant, wide-band absorption feature is present even without damping compensation (figure 8(d)), this spectral/angular feature narrows and bends when dye concentration is increased and damping is compensated for. On the other hand, while the effective damping of the structure is being compensated for ($\text{Im}(\epsilon)$ goes from ≈ 0.4 for 0 mM to $\approx 10^{-4}$ for 10 mM, at their respective zero-crossing point for $\text{Re}(\epsilon)$), absorption is still dramatically high because field localization is boosted. This conclusion is straightforward

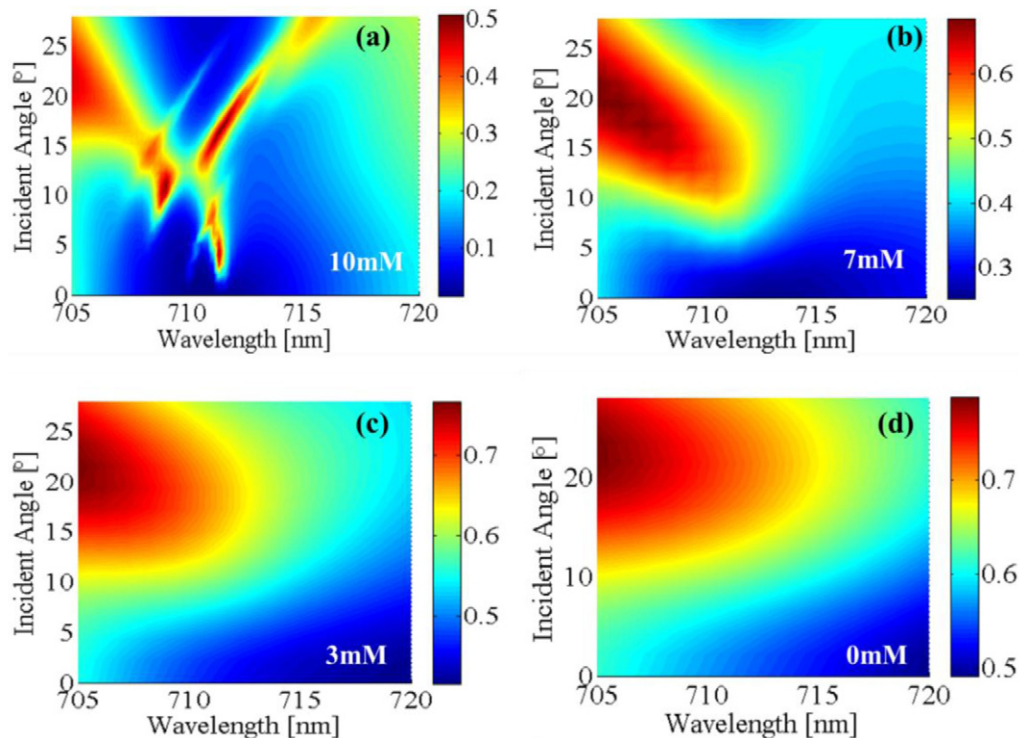


Figure 8. Full-wave calculations of absorption as a function of wavelength and incident angle for (a) 10 mM, (b) 7 mM, (c) 3 mM and (d) 0 mM of Rhodamine 800 dispersed in the silica cores of the nanoshells illustrated in figure 1. These results have been calculated by means of full-wave (finite element method) simulations.

if one considers that the absorption is proportional to the product $\text{Im}(\epsilon_{\text{eff}})|\mathbf{E}|^2$. However, high concentrations of dye molecules may impact overall damping compensation due to the presence of fluorescence quenching and other nonradiative phenomena [51]. The quenching effect leads to a reduction of gain in the system, although an analytical treatment of the molecule–nanoparticle interaction is probably needed to estimate its real impact. Alternative designs that, for example, use quantum dots [8] may be employed here.

An immediate consequence of the differences in field localization among the four structures with variable damping compensation is a variation in the strength of harmonic signal. In order to understand how critical is the introduction of proper gain (or alternatively, proper pumping condition) to the nonlinear response, we calculate forward and backward TH signals (arising from the metal shells only) from the four structures with absorption profiles in figure 8 where $\text{Re}(\epsilon) = 0$: $\lambda \approx 710.6$ nm for 10 mM (figure 9(a)), $\lambda \approx 714.3$ nm for 7 mM (figure 9(b)), $\lambda \approx 715.9$ nm for 3 mM (figure 9(c)) and $\lambda \approx 717.7$ nm for 0 mM (figure 9(d)). The detrimental effect induced by the reduction or complete elimination of the active material from the cores of the nanoshells is quite evident from an inspection of figure 9. A dramatic drop in TH efficiencies by about three orders of magnitude is observed when gain is eliminated. These results should also be compared with THG from a 5 nm thick gold film, which exhibits very similar angular behavior and conversion efficiency (figure 5(a)). The results shown in figure 9 demonstrate quite clearly how the introduction of gain in the metamaterial not only gives a different angular trend

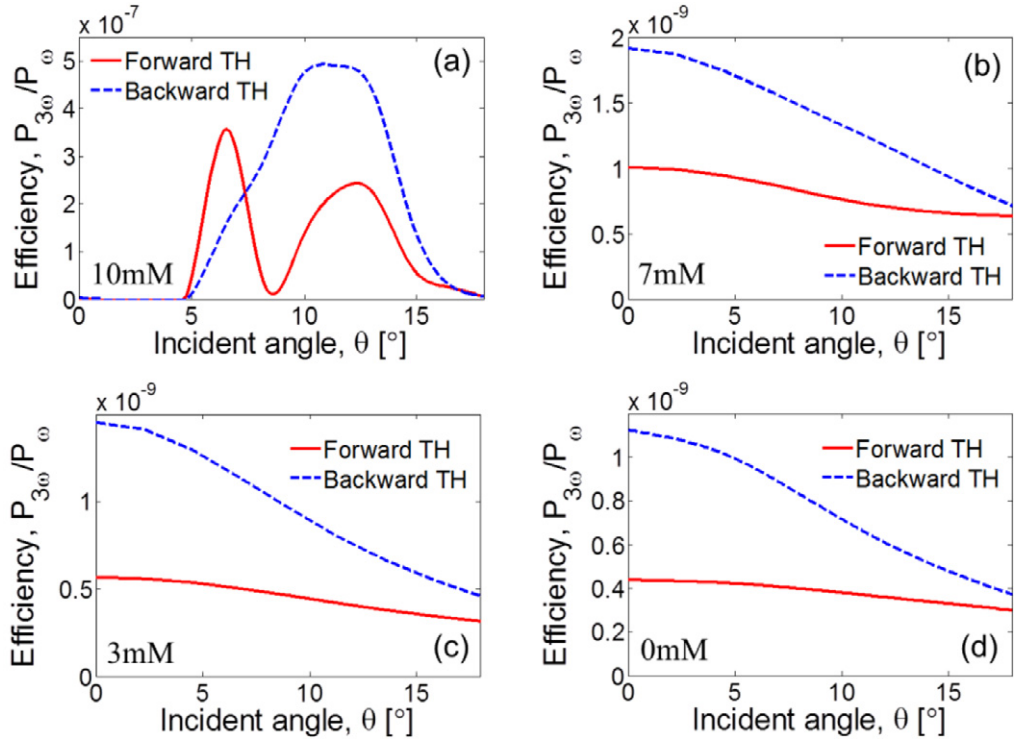


Figure 9. Forward and backward third harmonic conversion efficiency $\eta_{TH} = P_{3\omega}/P_{\omega}$ for the metamaterial described in section 2 with (a) 10 mM, (b) 7 mM, (c) 3 mM and (d) 0 mM of Rhodamine 800 dispersed in the cores of the nanoshells. The simulations are performed with a probe tuned at (a) $\lambda = 710.6$ nm, (b) $\lambda = 714.3$ nm, (c) $\lambda = 715.9$ nm and (d) $\lambda = 717.7$ nm, where the metamaterial's effective permittivity is $\text{Re}(\epsilon) = 0$. These results have been calculated by means of full-wave (finite element method) simulations.

to the generated signals but also improves significantly conversion efficiencies between two and three orders of magnitude. Similar results are also expected for SH generation.

6. Conclusions

We have studied SH and TH generation from metamaterials composed of plasmonic nanoshells working in a damping-compensation regime, to stress the ability of engineered materials exhibiting NZP properties to boost nonlinear processes. The introduction of a gain material into the cores of the nanoshells not only results in peculiar, narrow transmission, reflection and absorption features but also shapes dramatically the nonlinear response increasing both SH and TH efficiencies, which may be evaluated on a case-by-case basis for each resonant feature of the metamaterial. These results demonstrate how efficient, singularity-driven, low-threshold SH and TH generation processes may originate from the strong enhancement of the electric field achievable in metamaterials with NZP properties. Moreover, the investigation of both linear and nonlinear regimes performed by reducing the concentration of gain material or pump intensity proves the extreme sensibility of this regime to pump conditions and serves as a guide for future experimental works within the framework of damping compensation.

References

- [1] Pendry J, Holden A, Robbins D and Stewart W 1999 Magnetism from conductors and enhanced nonlinear phenomena *IEEE Trans. Microw. Theory Tech.* **47** 2075–84
- [2] Yen T J, Padilla W, Fang N, Vier D, Smith D, Pendry J, Basov D and Zhang X 2004 Terahertz magnetic response from artificial materials *Science* **303** 1494
- [3] Klein M W, Enkrich C, Wegener M, Soukoulis C M and Linden S 2006 Single-slit split-ring resonators at optical frequencies: limits of size scaling *Opt. Lett.* **31** 1259–61
- [4] Li J, Sun G and Chan C T 2006 Optical properties of photonic crystals composed of metal-coated spheres *Phys. Rev. B* **73** 075117
- [5] Yannopapas V 2007 Negative refractive index in the near-UV from Au-coated CuCl nanoparticle superlattices *Phys. Status Solidi (RRL)* **1** 208–10
- [6] Campione S, Albani M and Capolino F 2011 Complex modes and near-zero permittivity in 3D arrays of plasmonic nanoshells: loss compensation using gain [Invited] *Opt. Mater. Express* **1** 1077–89
- [7] Monti A, Bilotti F, Toscano A and Vegni L 2012 Possible implementation of epsilon-near-zero metamaterials working at optical frequencies *Opt. Commun.* **285** 3412–8
- [8] Campione S and Capolino F 2012 Composite material made of plasmonic nanoshells with quantum dot cores: loss-compensation and ϵ -near-zero physical properties *Nanotechnology* **23** 235703
- [9] Le F, Brandl D W, Urzhumov Y A, Wang H, Kundu J, Halas N J, Aizpurua J and Nordlander P 2008 Metallic nanoparticle arrays: a common substrate for both surface-enhanced Raman scattering and surface-enhanced infrared absorption *ACS Nano* **2** 707–718
- [10] Tserkezis C and Stefanou N 2011 Negative refraction in plasmonic crystals of metallic nanoshells *Metamaterials* **5** 169–77
- [11] Garcia N, Ponizovskaya E V and Xiao J Q 2002 Zero permittivity materials: band gaps at the visible *Appl. Phys. Lett.* **80** 1120–2
- [12] Silveirinha M and Engheta N 2006 Tunneling of electromagnetic energy through subwavelength channels and bends using ϵ -near-zero materials *Phys. Rev. Lett.* **97** 157403
- [13] Argyropoulos C, Chen P-Y, D'Aguanno G, Engheta N and Alù A 2012 Boosting optical nonlinearities in ϵ -near-zero plasmonic channels *Phys. Rev. B* **85** 045129
- [14] Ciattoni A, Rizza C and Palange E 2010 Extreme nonlinear electrodynamics in metamaterials with very small linear dielectric permittivity *Phys. Rev. A* **81** 043839
- [15] Vincenti M A, de Ceglia D, Ciattoni A and Scalora M 2011 Singularity-driven second- and third-harmonic generation at ϵ -near-zero crossing points *Phys. Rev. A* **84** 063826
- [16] Enoch S, Tayeb G, Sabouroux P, Guerin N and Vincent P A 2002 Metamaterial for directive emission *Phys. Rev. Lett.* **89** 213902
- [17] Lovat G, Burghignoli P, Capolino F, Jackson D R and Wilton D R 2006 Analysis of directive radiation from a line source in a metamaterial slab with low permittivity *IEEE Trans. Antennas Propag.* **54** 1017–30
- [18] Ciattoni A, Marinelli R, Rizza C and Palange E 2011 $|\epsilon|$ -near-zero materials in the near-infrared arXiv:1107.5540
- [19] Haus J W, Zhou H S, Takami S, Hirasawa M, Honma I and Komiyama H 1993 Enhanced optical properties of metal-coated nanoparticles *J. Appl. Phys.* **73** 1043–8
- [20] Scalora M, Vincenti M A, de Ceglia D, Roppo V, Centini M, Akozbek N and Bloemer M J 2010 Second- and third-harmonic generation in metal-based structures *Phys. Rev. A* **82** 043828
- [21] Owens D T, Fuentes-Hernandez C, Hales J M, Perry J W and Kippelen B A 2010 Comprehensive analysis of the contributions to the nonlinear optical properties of thin Ag films *J. Appl. Phys.* **107** 123114–8
- [22] Lepeshkin N N, Schweinsberg A, Piredda G, Bennink R S and Boyd R W 2004 Enhanced nonlinear optical response of one-dimensional metal-dielectric photonic crystals *Phys. Rev. Lett.* **93** 123902

- [23] Siegman A 1986 *Lasers* (Mill Valley, CA: University Science Books)
- [24] Sperber P, Spangler W, Meier B and Penzkofer A 1988 Experimental and theoretical investigation of tunable picosecond pulse generation in longitudinally pumped dye laser generators and amplifiers *Opt. Quantum Electron.* **20** 395–431
- [25] Wuestner S, Pusch A, Tsakmakidis K L, Hamm J M and Hess O 2010 Overcoming losses with gain in a negative refractive index metamaterial *Phys. Rev. Lett.* **105** 127401
- [26] Smith D R, Schultz S, Markoš P and Soukoulis C M 2002 Determination of effective permittivity and permeability of metamaterials from reflection and transmission coefficients *Phys. Rev. B* **65** 195104
- [27] Simovski C R 2009 On the extraction of local material parameters of metamaterials from experimental or simulated data *Theory and Phenomena of Metamaterials* ed F Capolino (Boca Raton, FL: CRC Press) p 8.1
- [28] Bohren C F and Huffman D R 1983 *Absorption and Scattering of Light by Small Particles* (New York: Wiley)
- [29] Steshenko S and Capolino F 2009 Single dipole approximation for modeling collections of nanoscatterers *Theory and Phenomena of Metamaterials* ed F Capolino (Boca Raton, FL: CRC Press) p 8.1
- [30] Campione S, Steshenko S, Albani M and Capolino F 2011 Complex modes and effective refractive index in 3D periodic arrays of plasmonic nanospheres *Opt. Express* **19** 26027–43
- [31] Jackson J D 1998 *Classical Electrodynamics* (New York: Wiley)
- [32] Markel V A, Pustovit V N, Karpov S V, Obuschenko A V, Gerasimov V S and Isaev I L 2004 Electromagnetic density of states and absorption of radiation by aggregates of nanospheres with multipole interactions *Phys. Rev. B* **70** 054202
- [33] Mackowski D W 1994 Calculation of total cross sections of multiple-sphere clusters *J. Opt. Soc. Am. A* **11** 2851–61
- [34] Fructos A L, Campione S, Capolino F and Mesa F 2011 Characterization of complex plasmonic modes in two-dimensional periodic arrays of metal nanospheres *J. Opt. Soc. Am. B* **28** 1446–58
- [35] Steshenko S, Capolino F, Alitalo P and Tretyakov S 2011 Effective model and investigation of the near-field enhancement and subwavelength imaging properties of multilayer arrays of plasmonic nanospheres *Phys. Rev. E* **84** 016607
- [36] Ewald P P 1921 The calculation of optical and electrostatic grid potential *Ann. Phys.* **64** 253–87
- [37] Ham F S and Segall B 1961 Energy bands in periodic lattices—Greens function method *Phys. Rev.* **124** 1786
- [38] Jordan K E, Richter G R and Sheng P 1986 An efficient numerical evaluation of the Green function for the Helmholtz operator on periodic structures *J. Comput. Phys.* **63** 222–35
- [39] Oroskar S, Jackson D R and Wilton D R 2006 Efficient computation of the 2D periodic Green's function using the Ewald method *J. Comput. Phys.* **219** 899–911
- [40] Celepcikay F T, Wilton D R, Jackson D R and Capolino F 2008 Choosing splitting parameters and summation limits in the numerical evaluation of 1-D and 2-D periodic Green's functions using the Ewald method *Radio Sci.* **43** RS6S01
- [41] Alù A, Silveirinha M G, Salandrino A and Engheta N 2007 Epsilon-near-zero metamaterials and electromagnetic sources: tailoring the radiation phase pattern *Phys. Rev. B* **75** 155410
- [42] Bloembergen N, Chang R K, Jha S S and Lee C H 1968 Optical second-harmonic generation in reflection from media with inversion symmetry *Phys. Rev.* **174** 813–22
- [43] Guyot-Sionnest P and Shen Y R 1988 Bulk contribution in surface second-harmonic generation *Phys. Rev. B* **38** 7985–9
- [44] Maystre D, Neviere M and Reinisch R 1986 Nonlinear polarisation inside metals: a mathematical study of the free-electron model *Appl. Phys. A: Mater. Sci. Process.* **39** 115–21
- [45] Heinz T F 1991 Second-order nonlinear optical effects at surfaces and interfaces *Nonlinear Surface Electromagnetic Phenomena* ed H Ponath and G Stegeman (Amsterdam: Elsevier) pp 353–416
- [46] Benedetti A, Centini M, Sibilio C and Bertolotti M 2010 Engineering the second harmonic generation pattern from coupled gold nanowires *J. Opt. Soc. Am. B* **27** 408–16
- [47] Boyd R W 2003 *Nonlinear Optics* (New York: Academic)

- [48] Rotenberg N, Bristow A D, Pfeiffer M, Betz M and van Driel H M 2007 Nonlinear absorption in Au films: role of thermal effects *Phys. Rev. B* **75** 155426
- [49] Renger J, Quidant R, van Hulst N and Novotny L 2010 Surface-enhanced nonlinear four-wave mixing *Phys. Rev. Lett.* **104** 046803
- [50] Ma H, Sheng P and Wong G 2002 Third-order nonlinear properties of Au clusters containing dielectric thin films *Optical Properties of Nanostructured Random Media* vol 82, ed V Shalaev (Berlin: Springer) pp 41–62
- [51] Dulkeith E, Morteani A C, Niedereichholz T, Klar T A, Feldmann J, Levi S A, van Veggel F C J M, Reinhoudt D N, Möller M and Gittins D I 2002 Fluorescence quenching of dye molecules near gold nanoparticles: radiative and nonradiative effects *Phys. Rev. Lett.* **89** 203002